IEEJ Journal of Industry Applications
Vol.8 No.3 pp.458–464 DOI: 10.1541/ieejjia.8.458

Paper

Influence of Structural Differences on Motor Characteristics of Concentrated Winding IPMSMs Obtained by Automatic Design

Akihiro Ura* Student Member, Masayuki Sanada*a) Senior Member
Shigeo Morimoto* Senior Member, Yukinori Inoue* Member

(Manuscript received July 19, 2018, revised Dec. 27, 2018)

Interior permanent magnet synchronous motors (IPMSMs) are widely used because of their high efficiency and high power. However, since their design has a high degree of freedom, application-specific design of IPMSMs is difficult. In this study, we investigate the structural characteristics of the models obtained by an automatic design system using a genetic algorithm (GA), and examine the structural factors useful in the design of IPMSMs that reduce eddy current loss in the stator and have high efficiency at high speeds. In addition, we confirm that by using this design method for the general shape of concentrated winding IPMSM, the eddy current loss is reduced and the efficiency is improved in the high-speed range.

Keywords: automatic design, genetic algorithm (GA), interior permanent magnet synchronous motor (IPMSM), eddy current loss

1. Introduction

Interior permanent magnet synchronous motors (IPMSMs) are widely used in various applications due to their high efficiency and high power. However, their design has a high degree of freedom, and structural differences in IPMSMs make a large effect on the motor characteristics [1]. Thus, application-specific design of an IPMSM generally requires experimental knowledge or many repeated calculations. Therefore, the simpler design methods and a shorter design process are being pursued [2].

To generalize the design of IPMSMs, design methods using various optimization algorithms have been proposed [3][4]. In particular, genetic algorithms (GAs) have many applications in the design of electromagnetic devices [5] and are widely applied in the design of IPMSMs [6]–[8].

In this study, a finite element method (FEM) was used for electromagnetic analysis of IPMSMs. The FEM can analyse high accuracy because taking magnetic saturation into account, so it is often applied for an electromagnetic field analysis of motors. However, FEM has the problem of generally requiring long computation times. To decrease design periods, coarse-mesh FEM, which uses a relatively small number of mesh elements, was proposed. In IPMSM analysis, the coarse-mesh FEM shows almost similar results compared to those obtained with fine-mesh FEM [9].

In this paper, first we describe the design of IPMSM structures that have high efficiency driving area as large as possible and fulfill maximum torque condition. The design was performed with an automatic design system using a combination of GA and coarse-mesh FEM. Then, we examine the structures of the motors obtained by automatic design to investigate which part of the structure affects the motor characteristics, especially for loss and efficiency.

In addition, by applying the obtained design method to general shape IPMSM, the efficiency improvement effect of the IPMSM is confirmed, and torque ripple is examined.

2. Design Model and Condition

The structure of the design model is shown in Fig. 1. The model has a concentrated winding stator with four poles and six slots. The motor size, current and voltage limit are used values which assumed air conditioner compressor driving. A total of nine design variables were evaluated, eight of which are shown in Fig. 1, and the other variable was x_5 (mm^3), the volume of each permanent magnet per pole. Since the stator slot size varies with changes in the stator structure, such as the tooth width x_7 and the yoke width x_8, the number of winding turns was changed to be approximately equal to the reference winding space factor shown in Table 1. The thickness of the flux barriers was the same as the width of the permanent magnets.

Table 1 shows the common specifications of the design

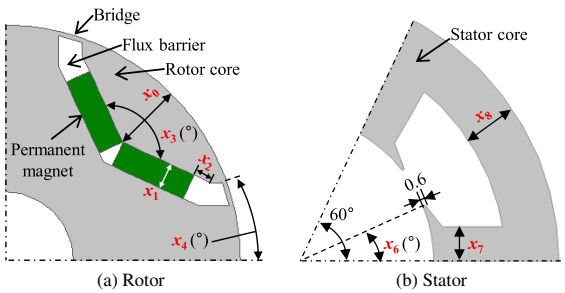

(a) Rotor (b) Stator

Fig. 1. Structure and design variables of IPMSM model (units: mm)

a) Correspondence to: Masayuki Sanada. E-mail: sanada@eis.osakafu-u.ac.jp
* Osaka Prefecture University
1-1, Gakuencho, Naka-ku, Sakai, Osaka 591-8531, Japan

Table 1. Common Specifications of the IPMSM model

Item (unit)	Value
Stator diameter (mm)	112.2
Rotor diameter (mm)	60
Rotor inner diameter (mm)	16
Stack length (mm)	60
Air gap length (mm)	0.5
Bridge width (mm)	0.5
Permanent magnet coercive force (kA/m)	915
Winding resistance (Ω/km)	23.33
Reference winding space factor (%)	50
Current limit (A)	4.4
Voltage limit (V)	100
Steel grade	35H300

Table 2. Design Variables

Item (unit)	Value	Number of Patterns	Step size
x_0 (mm)	5 – 20	16	1
x_1 (mm)	2.0 – 3.5	16	0.1
x_2 (mm)	1 – 8	8	1
x_3 (°)	30 – 180	16	10
x_4 (°)	10 – 25	16	1
x_5 (mm^3)	1560 – 2460	16	60
x_6 (°)	16 – 23	8	1
x_7 (mm)	3 – 10	8	1
x_8 (mm)	4 – 11	8	1

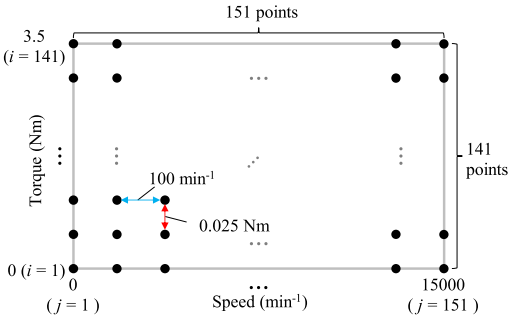

Fig. 2. Grid points in the efficiency map

model. The design variables were changed within the range of values shown in Table 2. Some combinations of design variables, it may be a combination that was impossible to make the motor structure. In that cases, the GA fitness of this individual was set to zero and excluded from the object of genetic operation.

To shorten the computation time, coarse-mesh FEM was utilized. The number of finite element meshes was set so that the rotor had approximately 3,000 elements and the stator had approximately 3,200 elements, both relatively small numbers.

In this study, the purpose of automatic design was to expand high efficiency driving area as much as possible while satisfying maximum torque condition. The GA fitness was set to the number of grid points where the efficiency was 93% or more in the efficiency map, shown in Fig. 2. The torque range was 0 to 3.5 Nm, and the torque step size was 0.025 Nm, which corresponds to $i = 1$ to 141. Similarly, the speed range was 0 to 15,000 min^{-1}, and the speed step size was 100 min^{-1}, which corresponds to $j = 1$ to 151. Therefore, the total number of grid points was 21,291. The maximum torque $T_{\max}$ of the design model was required to satisfy the constraint condition of exceeding 2.0 Nm. Thus, the fitness f of the GA and the constraint condition were as follows:

$$\text{maximize} \quad f = \sum_{i=1}^{141} \sum_{j=1}^{151} P_{ij} \quad \cdots\cdots\cdots\cdots\cdots\cdots \quad (1)$$

$$\text{subject to} \quad T_{\max} \geq 2.0$$

where P_{ij} is defined as follows:

$$P_{ij} = \begin{cases} 1, & \eta_{ij} \geq 93 \\ 0, & \eta_{ij} < 93 \end{cases} \quad \cdots\cdots\cdots\cdots\cdots\cdots\cdots\cdots \quad (2)$$

and η_{ij} is the efficiency at point (i, j) in the efficiency map (%). For all the operating points shown in Fig. 2, the combination of the current value and the current phase angle is selected at which the efficiency is the highest.

In this analysis, the GA was used to perform global search of the motor structure. The combinations of the nine design variables of motor structure were considered gene sequences. Five variables had gene lengths of 4 bits and four variables had gene lengths of 3 bits. Therefore, the total length of each gene was 32 bits and the total number of variable combinations was 2^{32}. Genetic operations were performed on those gene sequences to create new motor structures.

The GA parameters for this design process are shown in Table 3. To give an adequate diversity to the first generation, the population size per generation was set to 32 individuals. The selection methods were elite selection and tournament selection, to ensure that the high-fitness individuals in each generation are inherited to the next generation. To obtain a solution within a practical amount of time, the termination condition was set to 50 generations.

Table 3. GA Parameters

Item	Value
Population size	32
Crossover method	Uniform crossover
Crossover rate	60%
Mutation rate	15%
Selection method	Tournament selection + elite selection
Elite population size	2
Termination condition	50 generations

In this paper, electromagnetic field analysis and optimization software developed by our research group were used in the automatic design process. For calculation, Intel Core i5-4690 processor (3.5 GHz) 8 GB and 64 bit PC was employed.

3. Design Results and Considerations

The results of the automatic design are presented in this section. The calculation time of this design process was 189 hours and 57 minutes. At the last generation, the maximum fitness f is 1,606. The model that showed the highest fitness is called the GA-A model, and its rotor and stator structures are shown in Fig. 3.

For comparison, we consider one other structure obtained

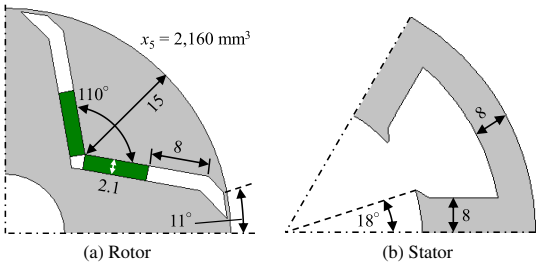

(a) Rotor (b) Stator

Fig. 3. GA-A model (units: mm)

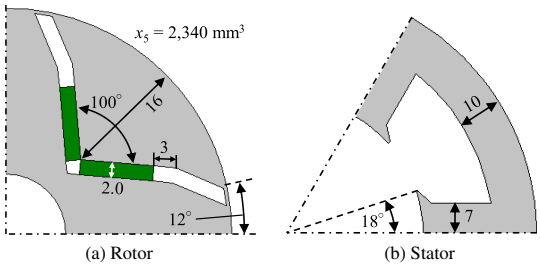

(a) Rotor (b) Stator

Fig. 4. GA-B model (units: mm)

Table 4. Comparison of characteristics of GA-A and GA-B

Item (Unit)	Value	
	GA-A	GA-B
Maximum torque T_{max} (Nm)	2.05	2.01
Magnet torque T_m (Nm)	1.71	1.73
Reluctance torque T_r (Nm)	0.34	0.29
Current phase β (°)	22.1	20.4
Armature flux linkage Ψ_o (Wb)	0.162	0.151
d-axis inductance L_d (mH)	10.58	8.45
q-axis inductance L_q (mH)	20.40	16.05
L_q - L_d (mH)	9.82	7.60
Minimum d-axis flux linkage Ψ_{dmin} (Wb)	0.04	0.05
Winding turns (per tooth)	126	114
Winding resistance (Ω)	0.624	0.575
Fitness f	1606	1258

by automatic design, although it exhibited relatively low fitness. This model is called GA-B, and its structures are shown in Fig. 4. The fitness of the GA-B model is 1,258. Both of the models have a V-shaped rotor, but the shape of their flux barrier is different.

Table 4 compares the model parameters for GA-A and B. Torque, current phase, armature flux linkage, and inductance values are for the maximum torque. Figure 5 shows efficiency maps for both models. Especially in the high-speed range, the operable and high-efficiency areas of the GA-A model are wider than those of GA-B.

To analyze the efficiency during operation, we set two points P_1 and P_2 on the efficiency map. Point P_1 is at high torque and low speed (T = 2.0 Nm and N = 2,000 min^{-1}), and point P_2 is low torque and high speed (T = 0.5 Nm and N = 6,000 min^{-1}). The loss details for both models at both points are shown in Fig. 6. At point P_1, there is no significant difference in loss between the two models. In contrast, at point P_2, copper and iron losses of the GA-A model were small compared to those of the GA-B model. Due to a smaller number of winding turns, the winding resistance of the GA-B model

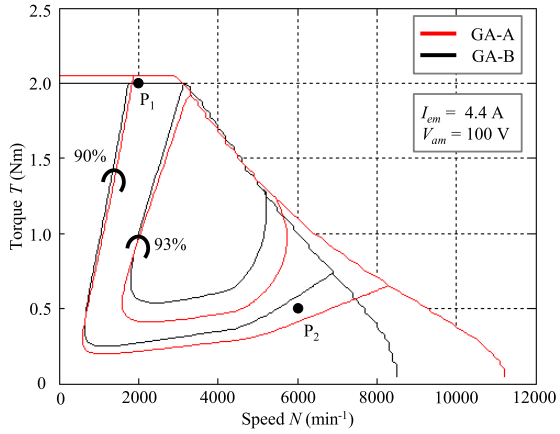

Fig. 5. Efficiency maps for GA-A and GA-B

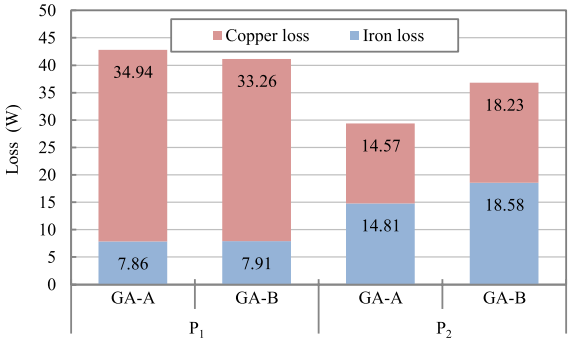

Fig. 6. Details of losses at points P_1 and P_2 in GA-A and GA-B

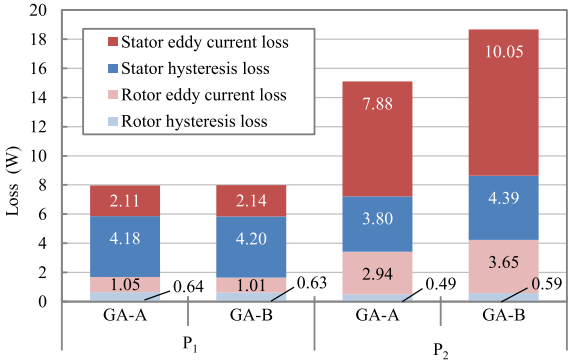

Fig. 7. Details of iron loss at points P_1 and P_2 in GA-A and GA-B

was lower, but it had a phase current of 3.25 A for driving at point P_2, which was larger than the 2.79 A seen in the GA-A model. Therefore, the copper loss of the GA-B model was larger.

Details of iron loss in both models are shown in Fig. 7. At point P_1, no significant difference is seen between both models, but at point P_2, the stator eddy current loss accounts for the largest iron loss in both models. The GA-B stator eddy current loss had the largest increase in comparison with the GA-A model. To investigate the position where the stator eddy current loss occurs, the distributions of eddy current loss are shown in Fig. 8. The stator eddy current loss is particularly large at the pole horn at the end of the stator tooth indicated by circles in the figure.

To consider whether high-efficiency operation at high

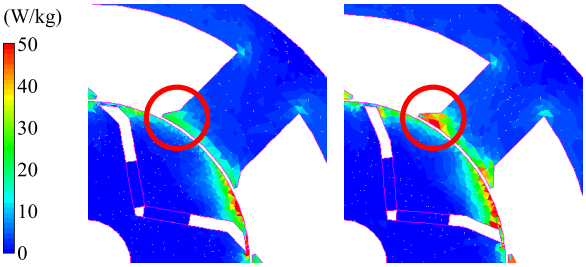

(a) GA-A (b) GA-B

Fig. 8. Eddy current loss distributions at point P_2 in GA-A and GA-B

Table 5. Comparison of Characteristics of All Four Models

Item (Unit)	Value			
	GA-A	GA-B	AR-BS	BR-AS
Maximum torque T_{max} (Nm)	2.05	2.01	1.82	2.27
Magnet torque T_m (Nm)	1.71	1.73	1.55	1.89
Reluctance torque T_r (Nm)	0.34	0.29	0.26	0.38
Current phase β (°)	22.1	20.4	20.6	22.0
Armature flux linkage Ψ_0 (Wb)	0.162	0.151	0.140	0.176
d-axis inductance L_d (mH)	10.58	8.45	8.36	10.53
q-axis inductance L_q (mH)	20.40	16.05	15.32	19.98
L_q - L_d (mH)	9.82	7.60	6.95	9.44
Minimum d-axis flux linkage Ψ_{dmin} (Wb)	0.040	0.053	0.042	0.050
Winding turns (per tooth)	126	114	114	126
Winding resistance (Ω)	0.624	0.575	0.575	0.624
Fitness f	1606	1258	1481	1340

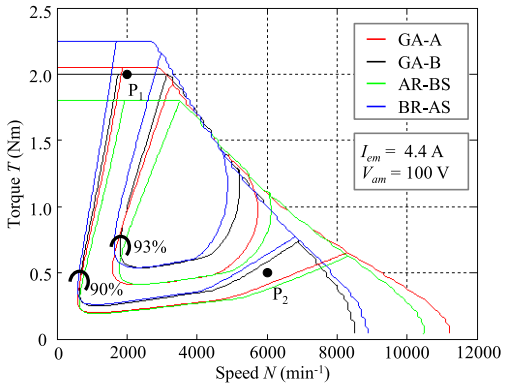

Fig. 9. Efficiency maps for all four models

speed in GA-A is mainly caused by the rotor or stator structure, we created models in which the rotor and stator of GA-A and GA-B were swapped. The model that combined the rotor of GA-A and the stator of GA-B is called AR-BS, and the model that combined the rotor of GA-B and the stator of GA-A is called BR-AS.

Table 5 compares the parameters of these additional models with those of GA-A and GA-B. As in the previous case, torque, current phase, armature flux linkage, and inductance values are at the maximum torque. The efficiency maps of all four models are shown in Fig. 9. In the AR-BS, the maximum torque was greatly decreased, but the high-efficiency operation area expanded in the high-speed, low-torque range.

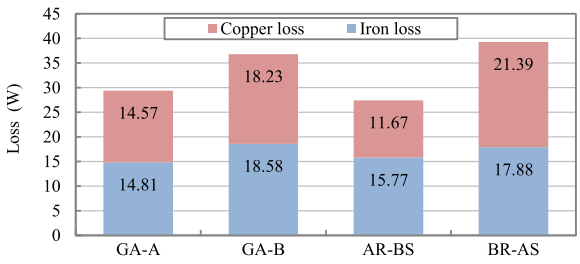

Fig. 10. Details of losses at point P_2 in all four models

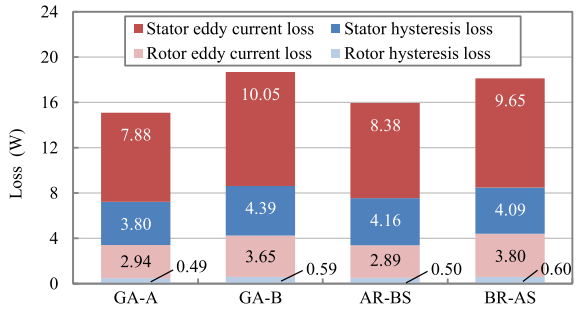

Fig. 11. Details of iron loss at point P_2 in all four models

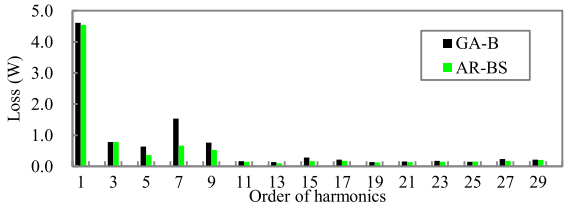

Fig. 12. Eddy current loss harmonics at point P_2 in GA-B and AR-BS

In contrast, in the BR-AS model, the maximum torque was larger, and the high-efficiency area expanded in the low-speed, high-torque range, but efficiency decreased at high speed. From this, we concluded that the rotor of the GA-A contributes significantly to the high-efficiency area expansion at high speed. In addition, the GA-A model shows that the high-efficiency area expanded in both the high-speed and low-speed ranges, making it a well-balanced model.

Figure 10 shows the details of losses at point P_2. In the AR-BS model, in which the rotor of GA-B was replaced by that of GA-A, both copper and iron losses decreased as compared to the GA-B. In contrast, in the BR-AS model, in which the stator of GA-B was replaced by that of GA-A, compared with the GA-B, iron loss was almost unchanged and copper loss increased. The change in copper loss is due to the reduction in the amount of current required to drive the same point as in the GA-A and GA-B models. To investigate the cause of the decrease in iron loss by the rotor structure, the details of iron loss were examined. Figure 11 provides details of the iron loss at point P_2, and it shows that, among the iron losses, the rotor change reduced the stator's eddy current loss the most.

Next, we examined how the difference in rotor structure affects stator eddy current loss. The stator eddy current losses calculated for each harmonic component for two models with different rotors, GA-B and AR-BS, are shown in Fig. 12. The figure shows that in the stator eddy current loss, the

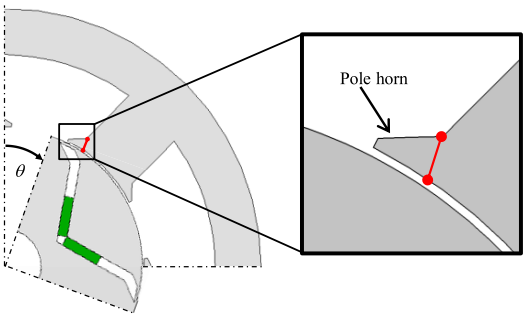

(a) The position where magnetic flux passing through is calculated.

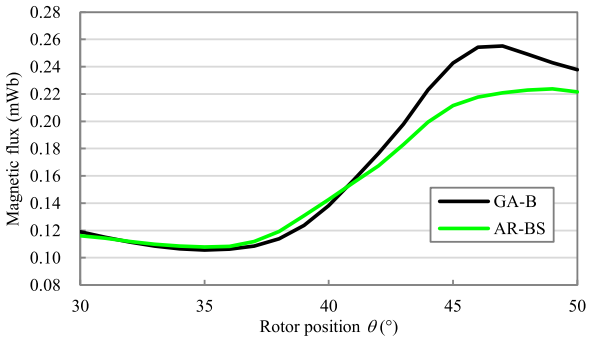

(b) Change in magnetic flux passing through stator pole horn.

Fig. 13. Magnetic flux passing through pole horn at point P_2 in GA-B and AR-BS

fundamental wave component is the largest and the fifth, seventh, and ninth harmonic components are greatly reduced due to the change of rotor structure. The eddy current loss is expressed by the following equation [10][11]:

$$W_e = \sum_{i=1}^{e}\left[m_i \sum_{k=1}^{n}\left\{k_e(kf)^2 B_{rk-i}^2 + k_e(kf)^2 B_{\theta k-i}^2\right\}\right] \cdots\cdots \quad (3)$$

where W_e is the eddy current loss (W), e is the number of elements in the region, m_i is the mass of the i-th element (kg), k_e is the eddy current loss coefficient, k is the harmonic order, n is the maximum harmonic order, f is the basis frequency (Hz), B_{rk-i} is the amplitude of the k-th harmonic order of the radial magnetic flux density of the i-th element (T), and $B_{\theta k-i}$ is the amplitude of the k-th harmonic order of the tangential magnetic flux density of the i-th element (T).

Equation (3) shows that a sharp change in the magnetic flux density caused the large harmonic component of the eddy current loss.

To observe how the magnetic flux density changes due to the difference in rotor structure, we focused on the flow of magnetic flux during rotation. The magnetic flux passing through the red line shown in Fig. 13(a) was calculated. The definition of rotation angle θ is also described in this figure. Figure 13(b) shows the magnetic flux passing through the pole horn when the flux barrier of the rotor overlaps the position of the pole horn of the stator in the same two models. The change of the magnetic flux in AR-BS is gentle compared to that of GA-B. Magnetic flux diagrams are shown in Fig. 14. In Figs. 14(a) and (b), when the rotation angle θ is 41°, the amount of magnetic flux flowing into the stator pole horn is almost same, as shown in Fig. 13(b). In contrast, in Figs. 14(c) and (d), at $\theta = 45°$ where a large difference occurs in the magnetic flux in Fig. 13(b), the magnetic path of the

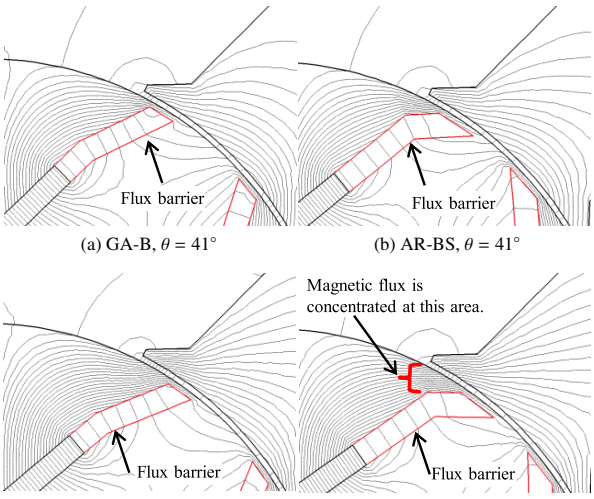

(a) GA-B, $\theta = 41°$ (b) AR-BS, $\theta = 41°$

(c) GA-B, $\theta = 45°$ (d) AR-BS, $\theta = 45°$

Fig. 14. Magnetic flux diagrams at point P_2

AR-BS is narrower than the GA-B due to the end of the flux barriers bending outwardly with respect to the magnets, and magnetic saturation occurs. As a result, for the AR-BS, the magnetic flux toward the stator gradually flows to the pole horns. This reduces the eddy current loss in the stator pole horn.

4. Applying Design Method to Standard IPMSM

In the previous section, we showed that the stator eddy current loss at high speed can be reduced by bending the flux barrier of the rotor outward with respect to the magnet.

Several studies on IPMSM structures that reduce the stator eddy current loss by changing the shape of the rotor flux barrier have been made so far. Yamazaki *et al.* designed the flux barrier of rotor inward with respect to the magnet on the rotor surface side for reduce spatial harmonics by permanent magnet, and reduce eddy current loss [12]. Unlike this design method, the design method in this paper is utilizing magnetic saturation caused by bending the flux barrier outwardly, and reduces stator eddy current loss. We applied this rotor structure to a standard IPMSM shape and confirmed that the stator eddy current loss is reduced.

The standard model to which this design was applied is shown in Fig. 15. It has a concentrated winding stator with four poles and six slots. The rotor is V-shaped, and the volume of the permanent magnet per pole is 2,520 mm^3. The parameters for motor size, magnet, steel grade, current, and voltage are the same as those in the automatic design model (Table 1). The winding has 117 turns per tooth. We developed four models by changing the flux barrier bending angle ϕ as shown in Fig. 16.

The efficiency maps for these models are shown in Fig. 17. As the angle ϕ increased, the high-efficiency area in the high-speed range expanded. The details of iron loss at point P_2 are shown in Fig. 18. The eddy current loss of the stator decreased as the angle ϕ increased and the eddy current loss at $\phi = 210°$ was approximately half of the eddy current loss at $\phi = 150°$.

These results confirmed that stator eddy current loss is reduced by increasing the angle of the flux barrier of the rotor.

Finally, we examined torque ripples of these models, which

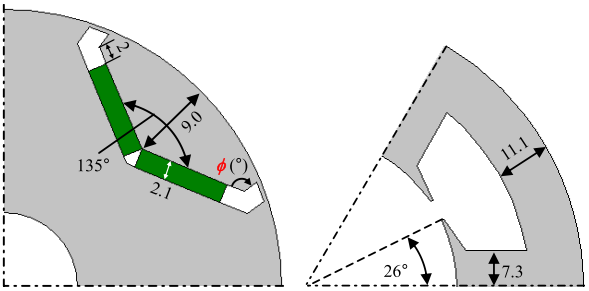

(a) Rotor (b) Stator

Fig. 15. Standard model (units: mm)

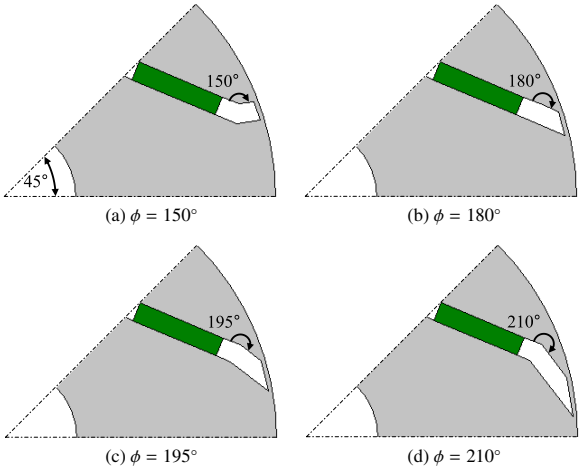

(a) ϕ = 150° (b) ϕ = 180°

(c) ϕ = 195° (d) ϕ = 210°

Fig. 16. Additional models with flux barrier variations

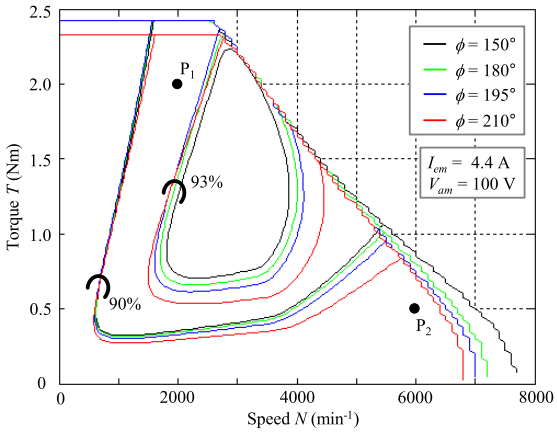

Fig. 17. Efficiency maps for flux barrier variations

Table 6. Torque ripple rate for flux barrier variations (units: %)

Flux barrier angle	ϕ=150°	ϕ=180°	ϕ=195°	ϕ=210°
At maximum torque	25.87	40.77	35.23	18.73
At P_1 (2.0 Nm, 2,000 min^{-1})	29.10	43.90	39.30	18.12
At P_2 (0.5 Nm, 6,000 min^{-1})	160.54	275.81	279.77	110.67

cause vibration and noise. The torque ripple rate at maximum torque and two points, P_1 and P_2 are shown in Table 6. Table shows the model of ϕ = 210° is suppressed torque ripple rate at maximum torque and point P_1. On the other hand, at point P_2, although the torque ripple rate of the model of ϕ = 210° is relatively small, the torque ripple rate is large in all models, so not suitable for practical use.

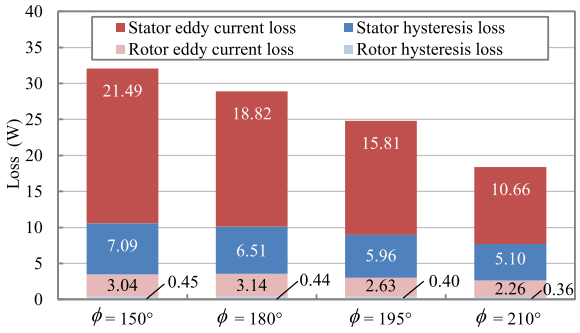

Fig. 18. Details of iron loss at point P_2 in flux barrier variations

5. Conclusion

In this study, we investigated the rotor and stator structure of IPMSM with wide high efficiency operation area by automatic design system using GA. Then, we focused on improvement of efficiency at high speed range and investigated in detail the structural features that reduce stator eddy current loss, which accounts for a large proportion of the loss. The results showed that certain rotor flux barrier shapes suppress a sharp increase in magnetic flux density at the stator pole horns, resulting in a decrease the eddy current loss. In addition, it was shown that this rotor flux barrier design improved the efficiency at high speed by being applied to standard concentrated winding IPMSM. Finally, we analyzed the torque ripple for the model applied this design method, and confirmed that the torque ripple is kept low in the low speed and high torque region. However, the torque ripple was large in the high speed and low torque region.

References

(1) K.C. Kim, J. Lee, H.J. Kim, and D.H. Koo: "Multiobjective Optimal Design for Interior Permanent Magnet Synchronous Motor", *IEEE Trans. on Magnetics*, Vol.45, No.3, pp.1780–1783 (2009)

(2) F. Parasiliti, M. Villani, S. Lucidi, and F. Rinaldi: "Finite-Element-Based Multiobjective Design Optimization Procedure of Interior Permanent Magnet Synchronous Motors for Wide Constant-Power Region Operation", *IEEE Trans. on Industrial Electronics*, Vol.59, No.6, pp.2503–2514 (2012)

(3) C. Lu, S. Ferrari, and G. Pellegrino: "Two Design Procedures for PM Synchronous Machines for Electric Powertrains", *IEEE Trans. on Transportation Electrification*, Vol.3, No.1, pp.98–107 (2017)

(4) P. Zhang, G.Y. Sizov, M. Li, D.M. Ionel, N.A. Demerdash, S.J. Dtretz, and A.W. Yeadon: "Multi-Objective Tradeoffs in the Design Optimization of a Brushless Permanent-Magnet Machine With Fractional-Slot Concentrated Windings", *IEEE Trans. on Industry Applications*, Vol.50, No.5, pp.3285–3294 (2014)

(5) J.A. Vasconcelos, R.R. Saldanha, L. Krahenbuhl, and A. Nicolas: "Genetic algorithm coupled with a deterministic method for optimization in electromagnetics", *IEEE Trans. on Magnetics*, Vol.33, No.2, pp.1860–1863 (1997)

(6) W. Zhao, F. Zhao, T.A. Lipo, and B.I. Kwon: "Optimal Design of a Novel V-Type Interior Permanent Magnet Motor with Assisted Barriers for the Improvement of Torque Characteristics", *IEEE Trans. on Magnetics*, Vol.50, No.11, 8104504 (2014)

(7) T. Nakata, M. Sanada, S. Morimoto, and Y. Inoue: "Automatic Design of IPMSMs Using a Genetic Algorithm Combined with the Coarse-mesh FEM for Enlarging the High-Efficiency Operation Area", IEEE Trans. on Industrial Electronics, Vol.64, No.12, pp.9721–9728 (2017)

(8) D. Lee, S. Lee, J.W. Kim, C.G. Lee, and S.Y. Jung: "Intelligent Memetic Algorithm Using GA and Guided MADS for the Optimal Design of Interior PM Synchronous Machine", *IEEE Trans. on Magnetics*, Vol.47, No.5 (2011)

(9) T. Nakata, M. Sanada, S. Morimoto, and Y. Inoue: "Automatic Design of IPMSMs Using a GA Coupled with the Coarse-mesh Finite Element Method", in Proc. ICEMS 2016, DS3G-1-11 (2016)

(10) S. Hashimoto, M. Sanada, S. Morimoto, and Y. Inoue: "Basic Study on the Suitable Structure of a Permanent Magnet Synchronous Motor with a Powder Magnetic Core", in Proc. IPEC 2014, 21P5-3 (2014)
(11) K. Yamazaki and Y. Seto: "Iron Loss Analysis of Interior Permanent-Magnet Synchronous Motors—Variation of Main Loss Factors Due to Driving Condition", *IEEE Trans. on Industry Applications*., Vol.42, No.4, pp.1045–1052 (2006)
(12) K. Yamazaki, M. Kumagai, T. Ikemi, and S. Ohki: "A Novel Rotor Design of Interior Permanent-Magnet Synchronous Motors to Cope with Both Maximum Torque and Iron-Loss Reduction", *IEEE Trans. on Industry Applications*, Vol.49, No.6, pp.2478–2486 (2013)

Akihiro Ura (Student Member) received the B.E. and M.E. degrees from Osaka Prefecture University, Sakai, Japan, in 2017 and 2019, respectively. He was involved in the study on the design of permanent magnet synchronous motors at Osaka Prefecture University. He is currently with Showa Denko K.K., Tokyo, Japan.

Masayuki Sanada (Senior Member) received the B.E., M.E., and Ph.D. degrees from Osaka Prefecture University, Sakai, Japan, in 1989, 1991, and 1994, respectively. Since 1994, he has been with the Graduate School of Engineering, Osaka Prefecture University, where he is currently an Associate Professor. His main areas of research interest are permanent-magnet motors for direct-drive applications, their control systems, and magnetic field analysis. Dr. Sanada is a member of the IEEE, the Japan Institute of Power Electronics, and the Japan Society of Applied Electromagnetics and Mechanics.

Shigeo Morimoto (Senior Member) received the B.E., M.E., and Ph.D. degrees from Osaka Prefecture University, Sakai, Japan, in 1982, 1984, and 1990, respectively. In 1984, he joined Mitsubishi Electric Corporation, Tokyo, Japan. Since 1988, he has been with the Graduate School of Engineering, Osaka Prefecture University, where he is currently a Professor. His main areas of research interest are permanent magnet synchronous machines, reluctance machines and their control systems. Dr. Morimoto is a member of the IEEE, the Society of Instrument and Control Engineers of Japan, the Institute of Systems, Control and Information Engineers, and the Japan Institute of Power Electronics.

Yukinori Inoue (Member) received the B.E., M.E., and Ph.D. degrees from Osaka Prefecture University, Sakai, Japan, in 2005, 2007, and 2010, respectively. Since 2010, he has been with the Graduate School of Engineering, Osaka Prefecture University, where he is currently an Associate Professor. His research interests include control of electrical drives, in particular, the direct torque control of permanent magnet synchronous motors and position sensorless control of these motors. Dr. Inoue is a member of the IEEE and the Japan Institute of Power Electronics.